Experimental Eye Research 205 (2021) 108499

Contents lists available at ScienceDirect

Experimental Eye Research

journal homepage: www.elsevier.com/locate/yexer

Super-resolution imaging of flat-mounted whole mouse cornea

Zhen Cai [a,1], Yang Zhang [a,1], Zheyuan Zhang [a], Ki-Hee Song [a], Lisa Beckmann [a], Ali Djalilian [b], Cheng Sun [c], Hao F. Zhang [a,*]

[a] Department of Biomedical Engineering, Northwestern University, Evanston, IL, 60208, USA
[b] Department of Ophthalmology, University of Illinois Chicago, Chicago, IL, 60612, USA
[c] Department of Mechanical Engineering, Northwestern University, Evanston, IL, 60208, USA

ARTICLE INFO

Keywords:
Super-resolution optical microscopy
Corneal endothelium
Single-molecule localization microscopy

ABSTRACT

Super-resolution microscopy revolutionized biomedical research with significantly improved imaging resolution down to the molecular scale. To date, only limited studies reported multi-color super-resolution imaging of thin tissue slices mainly because of unavailable staining protocols and incompatible imaging techniques. Here, we show the first super-resolution imaging of flat-mounted whole mouse cornea using single-molecule localization microscopy (SMLM). We optimized immunofluorescence staining protocols for β-Tubulin, Vimentin, Peroxisome marker (PMP70), and Histone-H4 in whole mouse corneas. Using the optimized staining protocols, we imaged these four intracellular protein structures in the epithelium and endothelium layers of flat-mounted mouse corneas. We also achieved simultaneous two-color spectroscopic SMLM (sSMLM) imaging of β-Tubulin and Histone-H4 in corneal endothelial cells. The spatial localization precision of sSMLM in these studies was around 20-nm. This work sets the stage for investigating multiple intracellular alterations in corneal diseases at a nanoscopic resolution using whole corneal flat-mount beyond cell cultures.

1. Introduction

Cornea, a transparent avascular connective tissue, plays an essential role in protecting the interior eye structures, contributing to the refractive power of the eye, and focusing light onto the retina with minimum optical scattering and degradation (Hart and Farrell, 1969; Maurice, 1962; Sridhar, 2018). The corneal epithelium, a stratified, nonkeratinizing squamous layer, creates the first barrier to the exterior environment. It is also an integral part of the tear film, critical to the eye's refractive power (DelMonte and Kim, 2011; Sridhar, 2018). The corneal endothelium, a single layer of hexagonal-shaped cells with severely limited proliferative capacities, plays a significant role in controlling the corneal transparency to maintain clear vision. The endothelial cells function as a permeable barrier that regulates the movement of aqueous humor into the hydrophilic stroma (DelMonte and Kim, 2011; Edelhauser, 2006; Sridhar, 2018). Because of their critical roles in maintaining normal functions of the eye, any pathological alteration may cause serious clinical problems. Therefore, understanding intracellular damages in corneal diseases is paramount (Aldrich et al., 2017; Anshu et al., 2012; Bashir et al., 2017; Janson et al., 2018; Shih et al., 2017). To this end, immunofluorescence (IF) based optical microscopy techniques have been widely used to study intracellular damages (Forest et al., 2015; He et al., 2011a). However, the spatial resolution of conventional microscopy technologies is fundamentally constrained by the optical diffraction limit (~200–300 nm in visible light spectral range), which prevents the visualization of molecular events and interactions related to pathological processes (Rust et al., 2006).

The invention of super-resolution localization microscopy (SMLM) techniques, including (Stochastic Optical Reconstruction Microscopy, STORM; Photoactivated Localization Microscopy, PALM; Points Accumulation for Imaging in Nanoscale Topography, PAINT) (Betzig et al., 2006; Hess et al., 2006; Rust et al., 2006) in the past decade permitted imaging of individual biomolecules and subcellular structures (Groβe et al., 2016; Salvador-Gallego et al., 2016) far beyond the optical diffraction limit. SMLM can further provide quantitative analysis at the molecular scale, including counting biomolecules, cluster sizing and analysis, and pair-wise distance measurement (Nicovich et al., 2017). Fig. 1A schematically illustrates the working principle of SMLM. Briefly, the biomolecules are first labeled with photoswitchable dyes to generate stochastic single-molecule fluorescence photoswitching ("blinkings")

* Corresponding author.
E-mail address: hfzhang@northwestern.edu (H.F. Zhang).
[1] These authors contributed equally to this work.

https://doi.org/10.1016/j.exer.2021.108499
Received 15 September 2020; Received in revised form 24 January 2021; Accepted 8 February 2021
Available online 18 February 2021

events in different frames (frame 1, 2, …, n in Fig. 1A). Second, all the single-molecule blinking events are captured by the camera, localized, and used for SMLM reconstruction (bottom of Fig. 1A). Specifically, every single-molecule blinking signal forms a pixelated, diffraction-limited point-spread-function (PSF) on the camera with system noises (Betzig et al., 2006). The PSF is then fitted with a model distribution, where the center location of the fitted PSF represents the location of this molecule. Because of various noises in SMLM, the localization process bears intrinsic uncertainty. The level of uncertainty (standard deviation, or σ), referred to as localization precision, can be either experimentally measured or analytically derived. σ is proportional to $1/\sqrt{N}$, where N is the emitted photon from the single emitter. σ is often used to quantify achievable resolution in SMLM, usually ~10–30 nm depending on the N of the dye and experimental conditions. Finally, the coordinates of all detected molecules are used to computationally render an SMLM image.

Furthermore, we (Dong et al., 2016) and other groups (Bongiovanni et al., 2016; Mlodzianoski et al., 2016; Zhang et al., 2015) developed spectroscopic SMLM (or sSMLM) techniques, which concurrently capture both the spatial and spectroscopic information of individual molecular fluorescence using an added dispersive element. Fig. 1B shows the schematics and working principle of an experimental sSMLM system. In addition to localizing single molecules in the same way as regular SMLM in the spatial images, the spectral images provide full emission spectral information of individual molecules, which further establishes the foundation for discriminating fluorescent species based on their distinct fluorescent emission spectra. Hence, sSMLM provides a unique opportunity to simultaneously image multiple fluorescent labels with even overlapping spectra and to further capture multi-molecular interactions in biological samples at the molecular level (Kim et al., 2017; Moon et al., 2017; Zhang et al., 2019).

Despite SMLM providing unprecedented optical imaging capabilities, the reported study on multi-molecular interactions using SMLM, including sSMLM techniques, has been mainly limited to cell cultures. The ability to image intact biological tissues has become highly desirable as it would enable investigating molecular-level alterations in individual cells in their natural local physiological environments. It would also permit investigating interactions among cells while preserving tissue integrity (Cheuk and Chan, 2004; He et al., 2011a; McGowan et al., 2007). To date, only a few studies reported SMLM of thin-sliced frozen tissues (Bon et al., 2018; Creech et al., 2017; Crossman et al., 2015; Kim et al., 2019; Klevanski et al., 2020; Spühler et al., 2016). To investigate the corneal endothelium, preparing thin-sliced frozen corneal samples is not an ideal method due to the ultrathin (<5 μm) cell monolayer (Del-Monte and Kim, 2011; He et al., 2011b; Sridhar, 2018). Besides, results from whole cornea imaging studies show rich heterogeneity information of the difference between central and peripheral corneal endothelial cells (Mimura and Joyce, 2006; Van den Bogerd et al., 2018), which are not available from the cultured cells. In this work, we developed experimental protocols to achieve multi-color super-resolution imaging of subcellular organelles and protein distributions in the flat-mounted whole cornea samples using sSMLM.

There are two major challenges in super-resolution imaging of whole-mount corneal tissue. First, the imaging quality in SMLM and

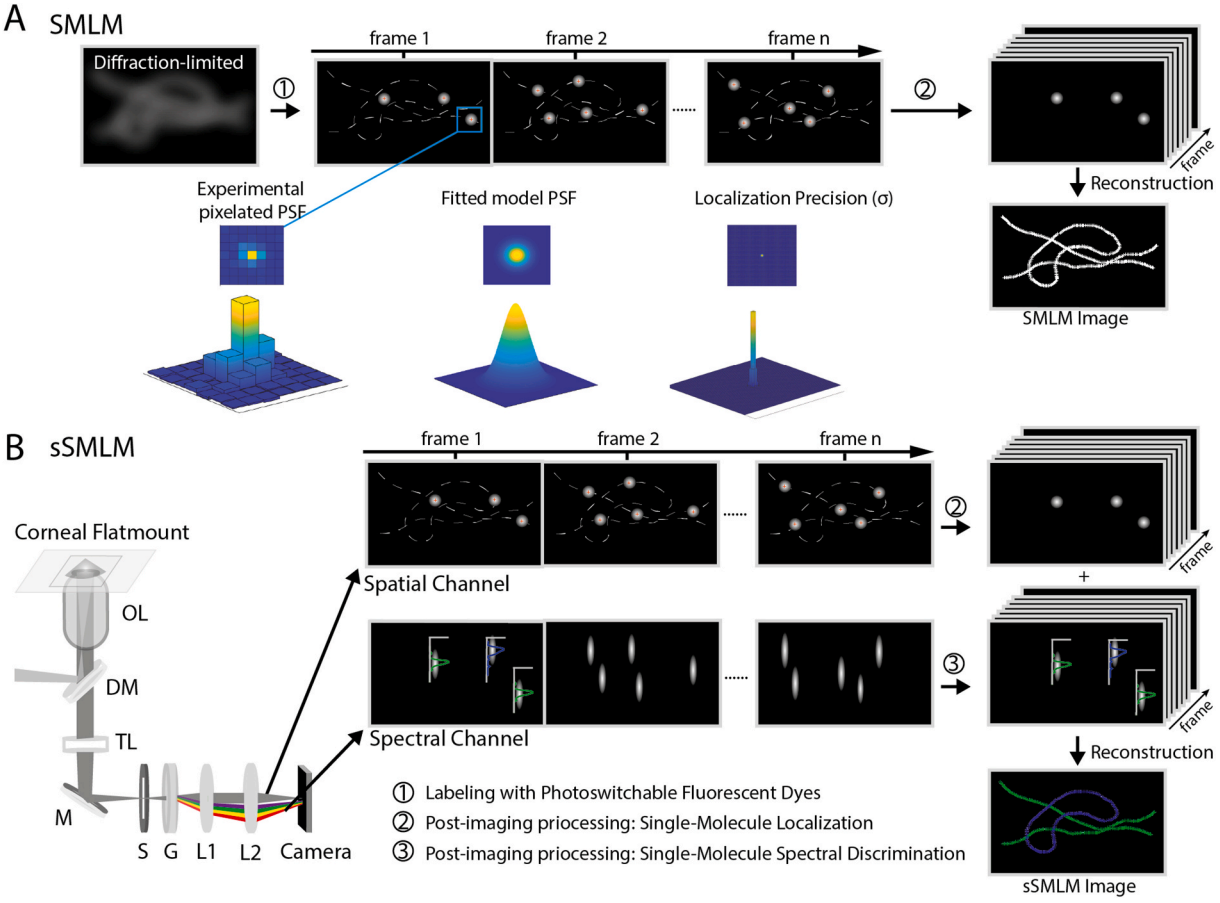

Fig. 1. (A) Illustration of SMLM principle: (top) the biomolecules are labeled with photoswitchable dyes to generate stochastic single-molecule fluorescence at different frames; the spatial coordinates of all detected single-molecule fluorescence are used to reconstruct an SMLM image; (bottom) the spatial location of every single molecule is localized by fitting its experimentally captured PSF. (B) Illustration of sSMLM principle: it has both spatial and spectral channels to simultaneously capture the spatial and spectral images of single molecules. In addition to the spatial localization using the spatial images, the spectral images provide additional full emission spectra of individual molecules. (OL: objective lens; DM: dichroic mirror; TL: tube lens; M: mirror; S: slit; G: grating; L1and L2: lenses 1 and 2).

sSMLM could be primarily affected by imaging artifacts, including fluorescence impurities, deviated background noises, and non-specific staining. Using sSMLM's spectral analysis function, we minimized the imaging artifacts from fluorescent impurity (Davis et al., 2018). We systematically investigated experimental noises' effect on sSMLM imaging recently (Song et al., 2018) and concluded that the spectral precision could reach ~3–4 nm for highly accurate spectral discrimination of single-molecule emissions. Thus, the main challenge for performing SMLM and sSMLM imaging of corneal flatmount is to identify optimal staining protocols to minimize the non-specific stainings (Jimenez et al., 2020). Second, the thickness of the cornea (~100 μm in mouse) (Henriksson et al., 2009) results in significant light attenuation and intracellular autofluorescence background in conventional SMLM using blue or green fluorescence detection (~400–600 nm) (Bates et al., 2007). To overcome this challenge, we conducted simultaneous multi-color sSMLM imaging within only a far-red spectral window (650–750 nm). Fluorescence imaging in the far-red spectral range effectively suppresses the autofluorescence background and enhances light penetration in biological tissues (Jun et al., 2017; Suseela et al., 2018).

This study systematically investigated immunofluorescence staining protocols on flat-mounted whole mouse cornea for SMLM imaging under various fixation and antibody-incubation conditions. We further optimized imaging conditions for both conventional SMLM and simultaneous two-color sSMLM. We show SMLM images of Tubulin, Vimentin, Peroxisome, and Histone proteins and two-color sSMLM images of simultaneously labeled Tubulin and Histone proteins in flat-mounted whole mouse cornea for the first time.

2. Materials & methods

2.1. sSMLM system overview and setup

The schematic of the SMLM/sSMLM optical system is shown in the left part of Fig. 1B. We immobilize fluorescence stained flat-mounted whole cornea between a rectangular No. 1.5 and a square No. 1 cover glasses. We filled the space between the cover slides with an imaging buffer (see section 2.5) and then mounted them onto the microscope's translational stage (Corneal Flatmount in Fig. 1B). We focused a 642-nm continuous-wave laser (MPB Communications) at the back focal plane of a Nikon Ti microscope body equipped with a perfect focus module. We used a neutral density filter to control the intensity of the incident light in the laser light path before focusing the light on the backport of the microscope. We acquired all SMLM and sSMLM images in a ~20 × 40 μm^2 FOV at a power density of 5.0 kW cm^{-2}. We used a 100 × Total Internal Reflection Fluorescence (TIRF) objective lens (CFI Apochromat 100 × , NA = 1.49, Nikon). We adjusted the illumination angle slightly smaller than the critical angle, which formed a highly inclined and laminated optical sheet (HILO) illumination mode. We collected the emitted fluorescence photons through the same objective lens. After passing through a tube lens (TL), the collected photons were routed by a mirror (M) to an entrance slit (S). We split the photons into the 0^{th}- and the 1st-order channels with a ratio of 1 : 3 using a transmission grating (G, 100 grooves/mm, STAR100, Paton Kawskely Education Ltd.). We detected both channels simultaneously to form the 0^{th}- and the 1st-order images, respectively representing the spatial and spectral images (Song et al., 2019; Zhang et al., 2019). The slit confines the field-of-view (FOV) of the spatial image. We adjusted the grating position relative to the imaging lens (L1, the focal length f = 50 mm) to achieve a spectral dispersion of 6 nm/pixel (Zhang et al., 2019). Emission signals in the 0^{th}-order (spatial channel in Fig. 1B) and 1st-order (spectral channel in Fig. 1B) channels were focused onto two different regions of an electron-multiplying charge-coupled device (EMCCD) camera (iXon 897, Andor) by an imaging lens (L2, f = 50 mm).

For single-color SMLM imaging, we removed the grating (G) to acquire only the spatial images. For two-color sSMLM imaging, we localized individual molecular spatial locations from the spatial images and analyzed the individual molecule's corresponding full emission spectra from the spectral images (Fig. 1B). As each fluorescent label has its unique spectral feature, we can discriminate different fluorescent labels based on their full emission spectra, which do not suffer from spectral overlapping, as illustrated in Fig. 1B (see section 2.5). This is particularly important for multi-color sSMLM imaging within the narrow far-red spectral window.

2.2. Mouse cornea harvesting

We used adult wild-type C57BL/6 mice aged 8–16 weeks and weighing 22–34 grams in this work. The mice were kept in the Center for Comparative Medicine at Northwestern University under normal lighting conditions with 12-h on and 12-h off cycles. We anesthetized the mice via intraperitoneal injection (10 mL/kg body weight) of a ketamine/xylazine cocktail (ketamine: 11.45 mg/mL; xylazine: 1.7 mg/mL, in saline). Then the health condition of the mouse eyes was monitored under an upright white-field microscope to exclude keratohelcosis, neovascularization, and anterior chamber infection. After euthanization by cervical dislocation, we cut the corneas from the eyeballs using ophthalmic corneal scissors all around the corneal limbus to ensure that no iris was attached.

2.3. Target proteins and antibodies

We first attempted to stain and image cytoskeletal proteins in endothelial cells of the cornea as their characteristic morphologies can be used to assess imaging quality unambiguously (Barry et al., 1995). We imaged β-Tubulin, a major protein for assembling tubulin filaments, and Vimentin, an intermediate filament, both present in all eukaryotic cells (Mikhaylova et al., 2015b). In addition to cytoskeletal proteins, we also imaged intranuclear protein Histone-H4 to visualize the nuclear envelope. Lastly, we imaged peroxisomal membrane protein 70 (PMP70) to visualize peroxisomes, which are single membrane subcellular organelles (Strauss et al., 2018). We summarize the primary antibodies in Table 1.

According to the animal source of primary antibodies, we used donkey anti-rabbit IgG and donkey anti-chicken IgY (Jackson ImmunoResearch) -Alexa Fluor 647 (AF647, Thermofisher) fluorescent antibodies conjugates for SMLM. For two-color sSMLM imaging, we used anti-rabbit IgG-AF647 and anti-chicken IgY-CF680 conjugates to simultaneously label β-Tubulin and Histone-H4, respectively. We prepared the secondary antibody conjugates using the N-hydroxysuccinimidyl coupling reaction, as we previously reported (Zhang et al., 2019).

2.4. Immunofluorescence staining protocol of flat-mounted whole cornea

Fig. 2 shows the overall flow of sample preparation. After removing the corneas from the eyeballs, we rinsed them once using 1x Phosphate Buffer Saline (PBS) and fixed them for 30 min using either 0.5% or 4.0% polyformaldehyde (PFA) based on the optimized staining protocol. We cut each cornea into four wedges to increase the number of cornea samples for testing at different labeling conditions. We permeabilized

Table 1
Primary antibodies used in this study.

Target protein	Host	Vendor	Catalog number	Optimized Dilution/ concentration
β-Tubulin	rabbit	Thermo Fisher	PA5-16863	1.0 μg/mL
Vimentin	chicken	Thermo Fisher	PA1-10003	1:5000
PMP70	rabbit	Thermo Fisher	PA1-650	2.0 μg/mL
Histone-H4	chicken	Abcam	Ab134212	2.5 μg/mL

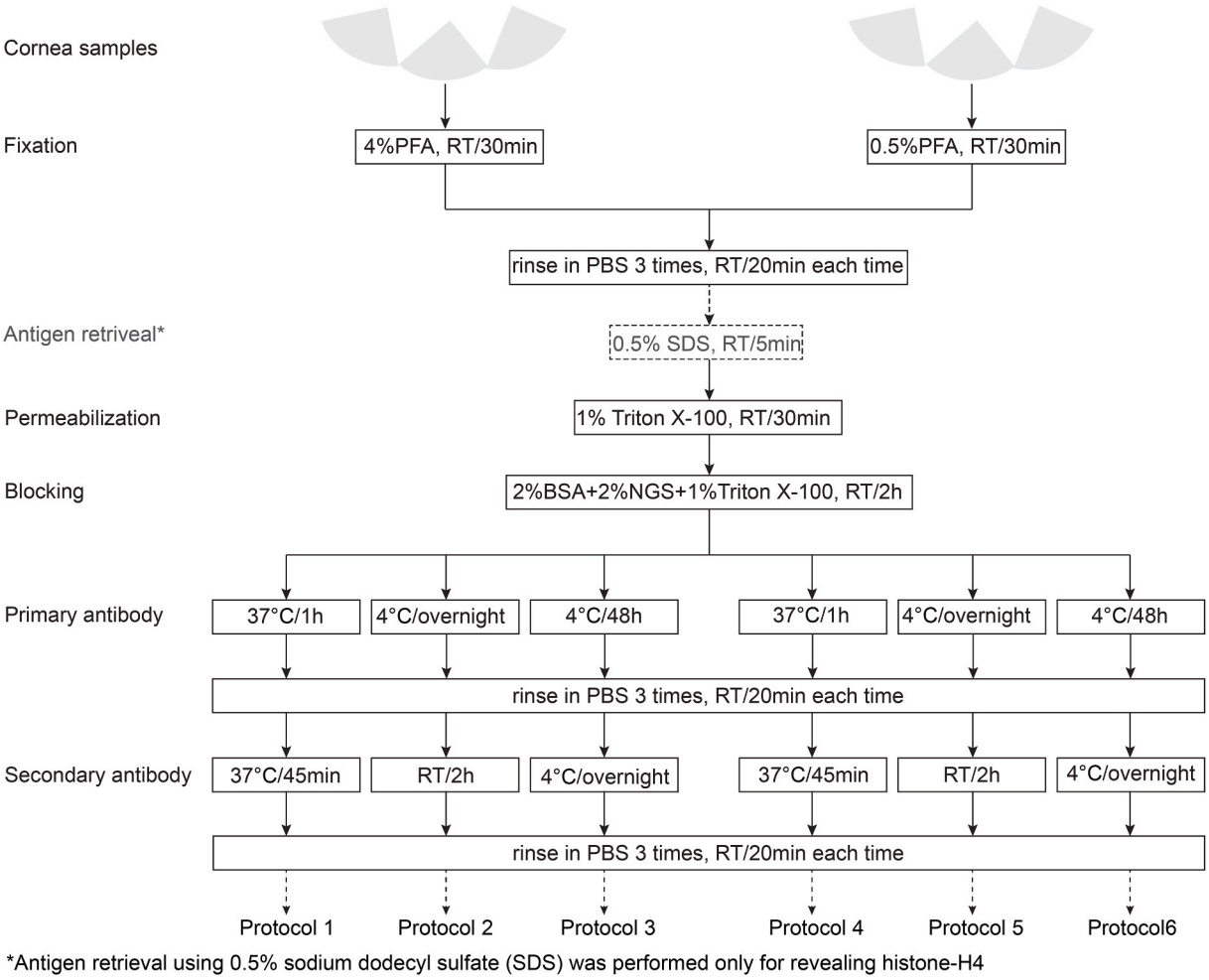

Fig. 2. Experimental design for 6 sample preparation protocols for flat-mounted whole corneas.

the corneas using 1% Triton 100-X in PBS at room temperature (RT) for 30 min. For Histone-H4 staining, antigen retrieval (AR) with 0.5% sodium dodecyl sulfate (SDS) in water for 5 min at RT was performed before permeabilization. The tissues were blocked with a blocking buffer containing 2% normal goat serum, 2% bovine serum albumin (BSA), and 1% Triton 100-X in PBS at RT for 2 h. The primary and secondary antibodies were diluted to concentrations listed in Table 1 in blocking buffer and then incubated with cornea tissues sequentially by one of the three incubation procedures: (1) primary antibody 60 min at 37 °C, secondary antibody 45 min at 37 °C; (2) primary antibody overnight at 4 °C, secondary antibody 2 h and RT; and (3) primary antibody 48 h at 4 °C, secondary antibody overnight at 4 °C. For two-color staining, we added the two primary antibodies simultaneously, followed by the two corresponding secondary antibodies. The samples were rinsed with PBS three times, 20 min each at RT after each fixation, primary antibody incubation, and secondary antibody incubation, as shown in Fig. 2.

After staining, we mounted the cornea samples on a rectangular No. 1.5 coverslip (22 mm × 60 mm) with the endothelial cells facing down according to the physiological curvature of the cornea. We gently flattened the corneas using ophthalmic micro forceps and covered them with a No. 1 square coverslip (22 mm). We used double-sided tapes to connect the two coverslips to form an imaging chamber and fill the chamber with imaging buffer, and sealed it with black nail polish.

2.5. Imaging acquisition and data processing

Prior to imaging, we freshly prepared an imaging buffer containing 50 mM Tris (pH = 8.0), 10 mM NaCl, 0.5 mg/mL glucose oxidase (Sigma, G2133), 2000 U/mL catalase (Sigma, C30), 10% (w/v) D-glucose, and 100 mM cysteamine. Then we added ~10 μL of the imaging buffer to fill up the chamber between the two coverslips. This specially developed imaging buffer is required to enable photoswitching during image acquisition. Particularly, SMLM dyes photoswitch between a bright state and a dark state in the presence of a triplet quencher (*e.g.,* Ethanolamine) and under a laser illumination power density of 5 kW cm^{-2}. Such a photoswitching process can typically last tens of minutes to a few hours with continuous illumination. Afterward, the illuminated dye molecules are permanently bleached. Please note that each FOV is relatively small (~20 × 40 μm^2) for capturing the images of 1–2 cells, and we typically capture ~10 FOVs for each imaging experiment. Considering the entire corneal flatmount contains thousands of cells, the corneal samples can be stored in PBS after imaging and be used for subsequent imaging of different cells.

The chambered coverslip system was sealed with black nail polish to prevent solution evaporation during the imaging process. We refilled the imaging buffer every hour if the data acquisition was not completed. The single-molecule blinking lasts for ~10–20 ms with ~500-8,000 photons in each blinking. Each recorded image frame's exposure time was 10 ms for single-color imaging and 20 ms for two-color imaging. We recorded 30,000 frames for each of the single-color SMLM and two-color sSMLM imaging reconstructions. To image endothelial cells, the imaging chamber (assembled as described in section 2.4) was mounted onto the objective lens with the rectangular cover glass side facing down. To image epithelial cells, the imaging chamber was flipped, and the square

cover glass side was facing down.

For single-color SMLM image processing, the imaging frame series were processed using ThunderSTORM (Ovesný et al., 2014). Specifically, we selected a B-Spline image filter, a peak intensity threshold of 1.2 × standard deviation with 8-neighborhood connectivity, and a fitting radius of 3 pixels. Our pixel size is 160 nm and the EM gain is 100. For two-color sSMLM image processing, we used RainbowSTORM, an ImageJ Plugin (Davis et al., 2020) to calibrate and process two-color imaging data as previously reported. The parameters for single-molecule localization are identical to the ones used for single-color imaging. For spectral discrimination, we selected the spectral detection spectral range from 650 nm to 750 nm, which passes at least 90% of the selected dye emissions while minimizing the noise uncertainty contribution on the intensity-weighted spectral mean of each blinking event. We calculated the intensity-weighted spectral mean (or spectral centroid) of each captured single-molecule emission spectrum and assigned each molecule with a spectral centroid between 682 nm and 688 nm as AF647 and between 702 nm 708 nm as CF680 molecules. The molecular misidentification rates among these two spectral windows are less than 1% (Zhang et al., 2019).

For epi-fluorescence imaging, images were acquired using the same optical setup as the sSMLM. Prior to SMLM imaging of each FOV, we reduced the laser power to 0.1 kW cm^{-2} using a neutral density filter to acquire the epifluorescence image at the same FOV as SMLM images.

For laser scanning confocal fluorescence imaging, we imaged corneal samples using a Leica SP5 confocal microscope. We used a 633-nm laser to excite the AF647 dye and detected the emission between 645 nm and 750 nm. We also performed deconvolution of the confocal microscopy results. We used the deconvolution Plugin in ImageJ software using the Lucy-Richardson Deconvolution method (Laasmaa et al., 2011). We generated a simulated PSF using the Born & Wolf Model (Nasse and Woehl, 2010) using a pixel size of 37 nm, an emission wavelength of 680 nm, and an N.A. of 1.4.

3. Results

3.1. Optimization of staining protocols for SMLM imaging

The optimization of the fluorescence labeling method is crucial for acquiring high-quality super-resolution images (Jimenez et al., 2020). There has been no report on immunofluorescence staining protocols of flat-mounted whole corneas for SMLM. Fixation and antibody incubation conditions have been shown to significantly affect immunofluorescence staining results in both conventional fluorescence imaging and super-resolution microscopy (Forest et al., 2015; He et al., 2011a). Thus, we investigated the fixation and antibody incubation steps for four proteins including β-Tubulin, vimentin, PMP70, and Histone-H4, as the target for SMLM imaging. These proteins have distinctive and characteristic morphologies for assessing staining quality and have been previously imaged using SMLM in cultured cells (Zhang et al., 2015).

We designed and investigated six protocols under various fixation and antibody incubation conditions by adapting the reported staining protocol for conventional fluorescence microscopy (Forest et al., 2015; He et al., 2011b) (Fig. 2). Specifically, we tested two fixation conditions at 4% and 0.5% PFA at RT. We further designed three antibody incubation conditions: (1) primary antibody 60 min at 37 °C and secondary antibody 45 min at 37 °C; (2) primary antibody overnight at 4 °C and secondary antibody 2 h at RT; (3) primary antibody 48 h at 4 °C and secondary antibody overnight at 4 °C. We qualitatively determined the SMLM imaging quality by observing the anticipated intracellular structure morphologies and assessing the scattered single-molecule signal levels for different protocols. The anticipated intracellular structure morphologies were compared with reported results in cultured cells (Xu et al., 2020; Zhang et al., 2015, 2019). We found that different protein marks require different protocols for optimal imaging quality. Specifically, β-Tubulin, Vimentin, and PMP70 require 4% PFA fixation, while Histone H4 requires 0.5% PFA fixation. Also, β-Tubulin, Vimentin, and Histone-H4 showed optimal imaging quality when incubating with primary antibody for 48 h at 4 °C and secondary antibody overnight at 4 °C while PMP70 requires the incubation of primary antibody for 60 min and secondary antibody for 45 min at 37 °C. Notably, Histone-H4 also requires an antigen retrieval step with SDS. We provide the single-color imaging quality assessments of the six protocols using β-Tubulin as an example in Fig. S1 and further discussion in Supplementary Note 1. In short, we found that Protocol 3 is optimal for labeling β-Tubulin and Vimentin; Protocol 1 is optimal for labeling PMP70; and Protocol 6 is optimal for labeling Histone-H4 on flat-mounted whole mouse cornea (Table 2).

3.2. Single-color SMLM imaging of mouse cornea flatmount

After the staining optimization, we compared the imaging qualities of SMLM and confocal microscopy in imaging β-tubulin under identical staining condition and FOV of 20 × 40 μm^2 (Fig. 3). We used 100 × oil immersion objective in confocal microscopy to match SMLM's objective magnification. Fig. 3A and B are confocal microscopy images before and after deconvolution, and Fig. 3C is the sSMLM image. Fig. 3D–F are magnified views of the highlighted areas in their corresponding original images. Fig. 3F shows the improved image quality contributed by higher spatial resolution. We compared the measured widths of a selected single microtubules (highlighted by the yellow lines in Fig. 3D–F) in Fig. 3G. The full-width-at-half-maximum (FWHM) of the microtubules size measured by confocal microscopy before and after deconvolution and SMLM are 259 nm, 177 nm, and 90 nm, respectively. The histogram of localization precision among 10^6 single molecules detected in Fig. 3C shows a peak at 10 nm, translating to an achievable spatial resolution of SMLM is ~25–40 nm under our experimental condition (Fig. 3H). Considering that the actual thickness of the Tubulin (plus attached primary and secondary antibodies) is ~70 nm and the localization precision of SMLM, our measured FWHM of 90 nm by SMLM closely matches the expected width of tubulin and agrees with a literature report (Mikhaylova et al., 2015a).

Next, we showed the SMLM images of β-Tubulin, Vimentin, PMP70, and Histone-H4 using their respective optimal staining protocols. To minimize artifacts when acquiring images using different microscopy systems and show the imaging performance of SMLM compared with conventional diffraction-limited microscopy, we acquired epifluorescence images (resolution = ~300 nm) of the identical FOV before acquiring the corresponding SMLM images. The epifluorescence images were captured using the SMLM setup with significantly lower illumination power (~0.1 kW cm^{-2}), which cannot drive the dye photoswitching process but is sufficient to generate regular fluorescence images.

Epifluorescence images (Fig. 4A1-4D1) showed intracellular structures of all labeled protein targets but were unable to resolve the nanoscale features of fibers or protein clusters. In comparison, SMLM images (Fig. 4A2-4D2) visualized the nanoscale architectures of the four protein targets. Fig. 4A3-4D3 are magnified views of the areas respectively highlighted by the squares in Fig. 4A2-4D2. Specifically, both β-Tubulin (Fig. 4A2 & 4A3) and vVmentin (Fig. 4B2 & 4B3) are abundantly expressed in endothelial cells with characteristic fibrous networks. Further, the distribution of Peroxisome marker PMP70 (Fig. 4C2 & 4C3) demonstrated elongated worm-like patterns in the cytoplasm. Lastly, the nuclear marker Histone-H4 exclusively resided in the nuclear envelope of the endothelial cells with a cluster-like shape distributed among the whole nucleus. Indeed, Histone-H4 is one of the basic nuclear proteins responsible for nucleosome structures. Visualizing these Histone-H4 clusters with diameters of hundreds of nanometers indicated that the high-order chromatin structures could be observed by SMLM in whole-mount tissue samples (Xu et al., 2020) instead of individual cultured cells.

We further tested SMLM imaging of the outer epithelial layers in the

Table 2
Summary of sSMLM imaging quality evaluation.

Targets	Protocol 1	Protocol 2	Protocol 3	Protocol 4	Protocol 5	Protocol 6
β-Tubulin	+	+	++	–	+	+
Vimentin	–	+	++	–	–	+
PMP70	++	+	+	+	–	–
Histone-H4	–	–	+	+	+	++

"-": no distinct morphologies; "+": ambiguous morphologies with scattered single molecule signals; "++": distinct morphologies with minimal scattered signal molecule signals.

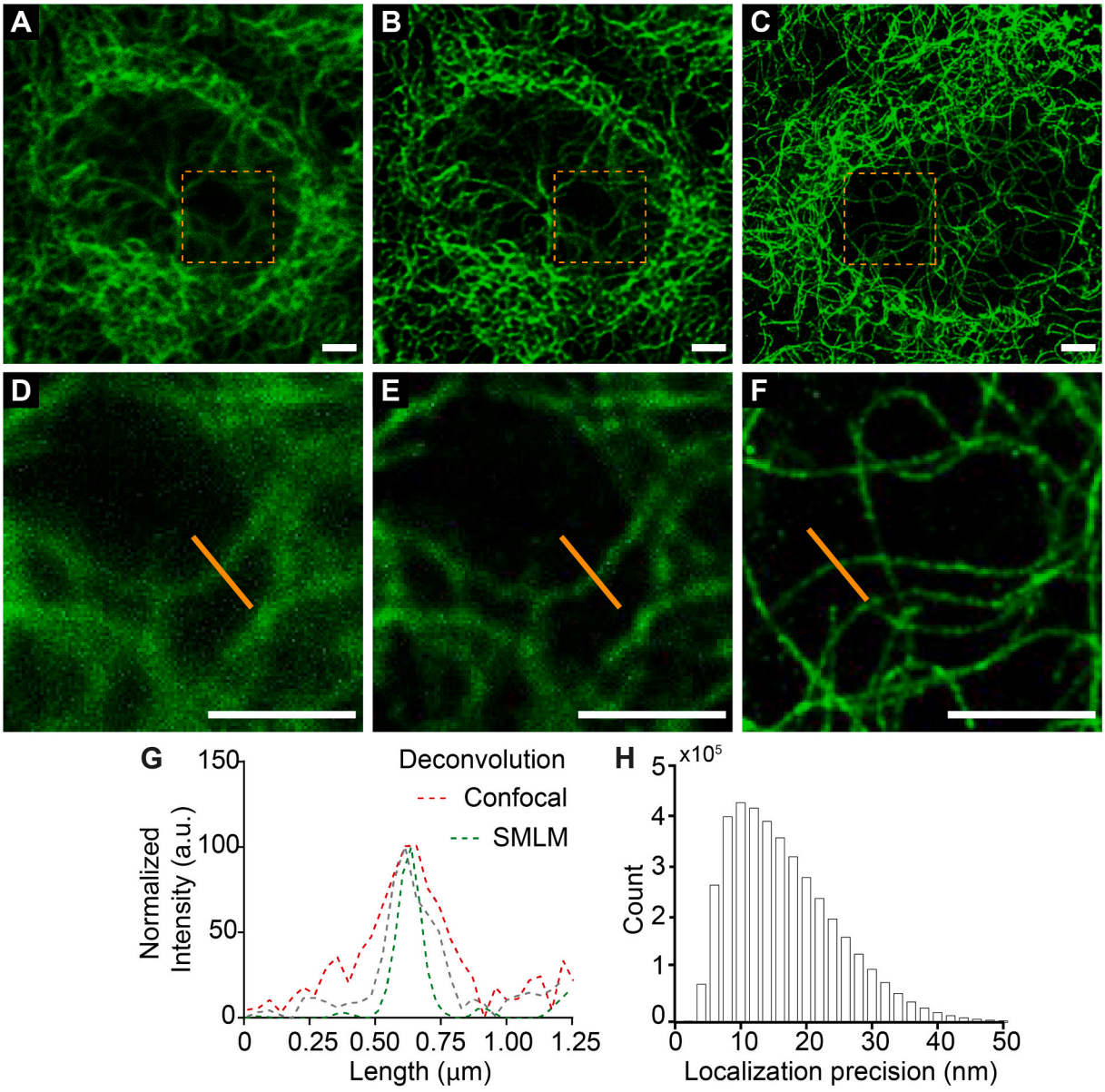

Fig. 3. Comparisons of confocal microscopy (**A, D**), deconvoluted confocal microscopy (**B, E**), and SMLM (**C, F**) images of corneal flatmount samples. **D-F** are the magnified views of the yellow-dashed boxes in **A-C**, respectively; (**G**) intensity profiles (gray: deconvolution; red: confocal; green: SMLM) of the lines in **D-F**, respectively; (**H**) histogram of localization precisions among 10^6 single molecules from detected in **C**; scale bar = 2 μm. (For interpretation of the references to color in this figure legend, the reader is referred to the Web version of this article.)

flat-mounted whole cornea using the optimized protocol for the endothelium described above. We stained and imaged β-Tubulin, PMP70, and Histone-H4 (Fig. 5). We observed consistent morphological features and imaging qualities in the epithelial cells compared to those in the endothelial cells. We also imaged the inner epithelial layers using wide-field illumination as the thickness of the epithelial layer over is 5 μm. In this condition, we observed a five-to ten-fold increase in cellular fluorescence background, which significantly degraded imaging quality. Better technologies to confine the illumination in the axial direction may help to further reduce the background to image inner epithelial layers (Chen et al., 2014).

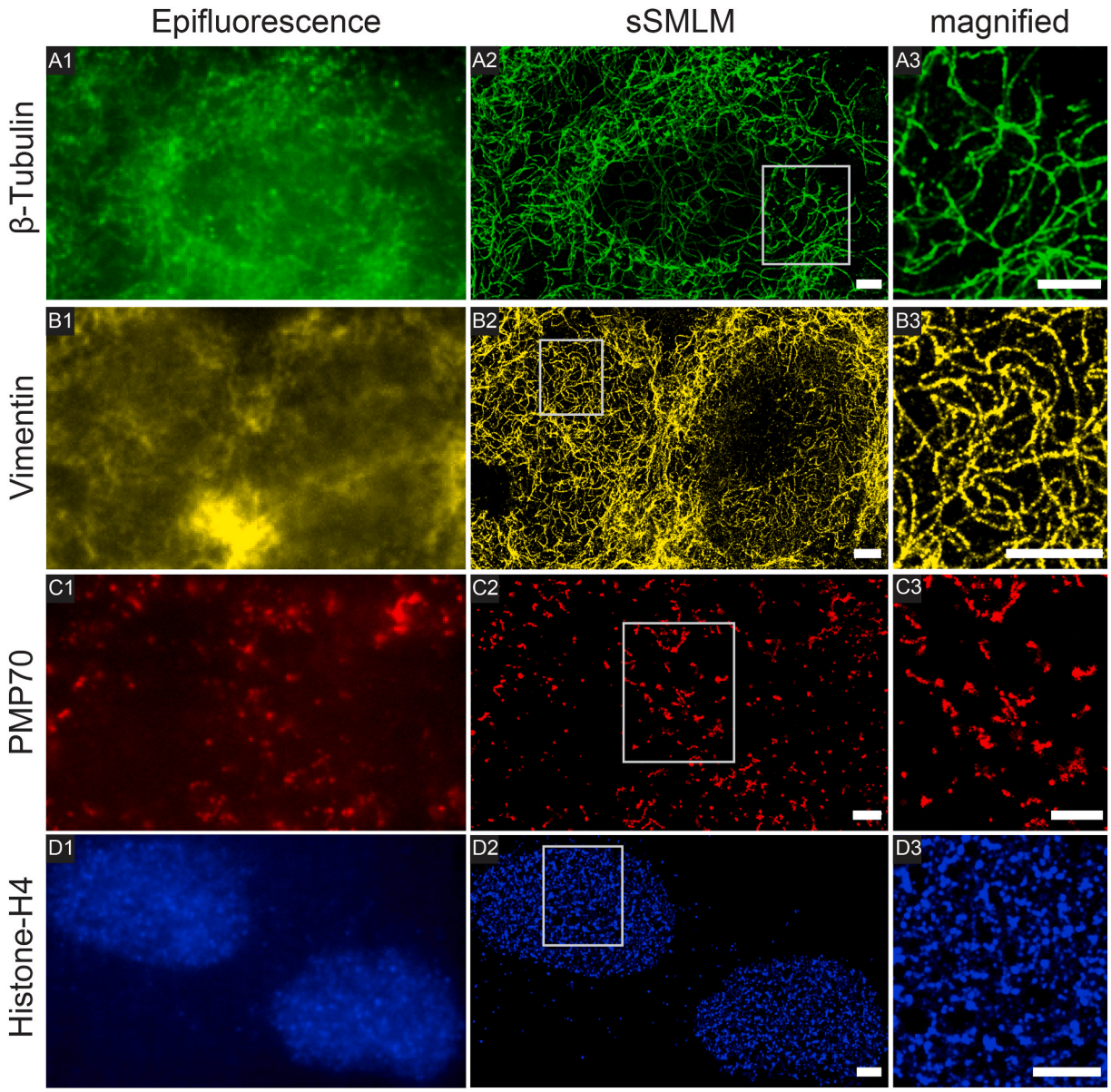

Fig. 4. Comparison between conventional epifluorescence and sSMLM images of the same corneal tissue samples. Epifluorescence images (**A1**-**D1**) and sSMLM images (**A2**-**D2**) of endothelial cells in flat-mounted whole mouse cornea stained with β-Tubulin (Protocol 3), Vimentin (Protocol 3), PMP70 (Protocol 1), and Histone-H4 (Protocol 6), respectively. The magnified views (**A3**-**D3**) better visualize the structures highlighted by the white boxes in panel **A2**-**D2**. Scale bar: 2 μm.

3.3. Simultaneous multi-color sSMLM imaging in the far-red channel

Because sSMLM can capture both spatial and spectral information of every single-molecule blinking, it allows us to resolve, in principle, an unlimited number of fluorescent labels (or color channels) simultaneously by analyzing spectral signatures of fluorescence labels (Dong et al., 2016). We demonstrated simultaneous multi-color sSMLM imaging of cultured cells (Song et al., 2019; Zhang et al., 2019) within the far-red spectral range. Such multiplexing imaging capability in the far-red spectral range may offer unique advantages in tissue imaging. Here, we validated simultaneous multi-color sSMLM imaging in flat-mounted whole mouse corneas using β-Tubulin and Histone-H4, which show distinct subcellular locations and morphologies. Since β-Tubulin and histone-H4 stainings required different PFA concentrations for fixation, we fixed the corneal tissue at 0.5%, 1%, 1.8%, 2.6%, 3.4%, and 4% PFA to identify optimal PFA concentration for simultaneous dual-label staining. We found that fixation at 1% PFA could maintain satisfactory imaging qualities for both β-Tubulin and Histone-H4. We further labeled β-Tubulin and Histone-H4 with AF647 and CF680 respectively in the same corneal sample.

The two fluorescent dyes have been previously used for simultaneous two-color sSMLM imaging (Zhang et al., 2019), although they have an emission spectral peak separation of only 30 nm with largely overlapping spectra (Fig. 6A). This is because sSMLM allows the detection of the full emission spectrum of every single molecule and discriminates AF647 and CF680 by determining their distinct spectral centroids (dashed lines in Fig. 6A). After imaging acquisition, we used RainbowSTORM to perform post-imaging analysis (see section 2.5) (Davis et al., 2020). Particularly, the two-color sSMLM image of β-Tubulin and Histone-H4 showed consistent morphological features compared to the SMLM images (Fig. 4). Note that two-color imaging qualities were slightly degraded as the optimized immunostaining protocol of the two-color imaging was a trade-off between the respective optimal staining protocols for Histone and Tubulin. In comparison, the sSMLM imaging reconstruction only using the spatial channel, which represents conventional SMLM imaging without spectroscopic analysis, fails to

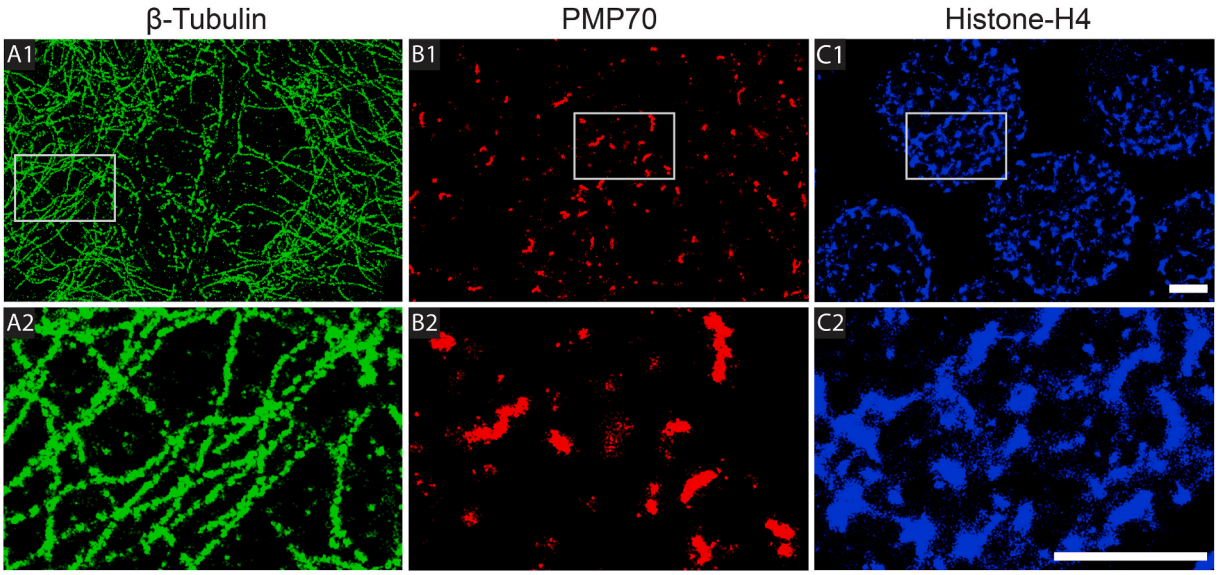

Fig. 5. sSMLM images of epithelial cells on flat-mount whole mouse cornea stained with β-Tubulin (**A1**), PMP70 (**B1**), and Histone-H4 (**C1**), respectively. The magnified views (**A2**, **B2**, **C2**) better show these structures in the white rectangular box in panel **A1**-**C1**. The staining protocols were the same as the ones optimized for endothelium. Scale bar: 2 μm.

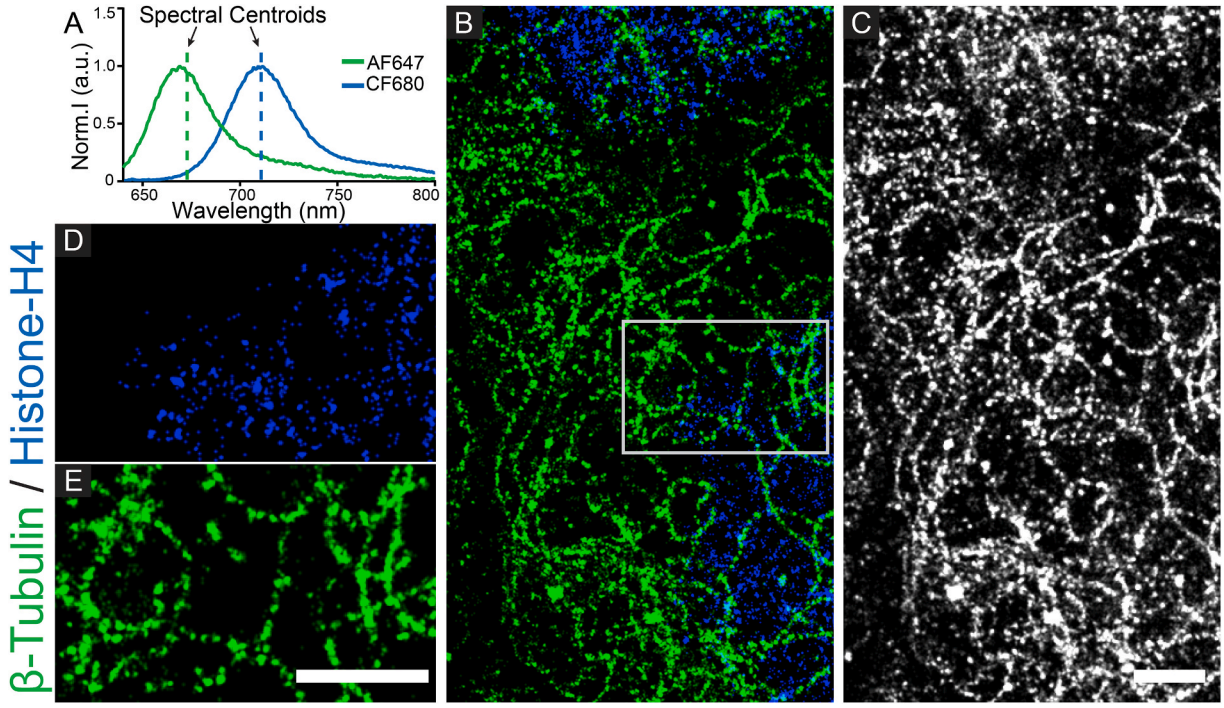

Fig. 6. Simultaneous two-color sSMLM imaging of the endothelial cells layer in the whole-mount corneal samples stained with β-Tubulin (green) and Histone-H4 (blue). (**A**) normalized averaged single-molecule emission spectra of AF647 and CF680 (green and blue curves) as well as their respective calculated spectral centroid indicated by the dashed lines; (**B**) overlaid two-color (green: AF647 channel; blue: CF680 channel) image; (**C**) conventional SMLM image; (**D**) magnified view of the Histone-H4 image from the highlighted region in panel **B**; (**E**) magnified view of the β-Tubulin image from the highlighted region in panel **B**. Scale bar: 2 μm. (For interpretation of the references to color in this figure legend, the reader is referred to the Web version of this article.)

distinguish the two fluorescent labels for two-color super-resolution imaging.

4. Discussion

The imaging qualities of SMLM, including sSMLM, heavily rely on the specificity of fluorescent labels to the biomolecular targets. Immunofluorescence labeling via antigen-antibody recognition is the most commonly used staining method for SMLM. Compared with conventional fluorescence microscopy (*e.g.,* epifluorescence or confocal microscopy), SMLM requires more stringent labeling protocols to preserve subcellular ultrastructures, reduce cellular autofluorescence, and minimize non-specific labeling. This is because SMLM requires higher illumination power and provides single-molecule sensitivity. Depending on the biomolecule of interest, the staining protocols are optimized case by case.

The literature suggests that the optimal staining methods for conventional fluorescence imaging of different protein targets in endothelial cells on flat-mounted whole cornea varied in their fixation (Forest et al., 2015; He et al., 2011a, 2016) and antibody incubation conditions (Bhogal et al., 2017; Chang et al., 2018; Quiroz-Mercado et al., 2016). We also found that both fixation and antibody-incubation conditions had significant impacts on the immunofluorescence staining and SMLM imaging qualities. In this work, we used only healthy corneal samples to rule out any potential influence from pathological alterations on the imaging quality and to focus on developing sSMLM technique in corneal flatmount. Here we discussed the influence of these two steps on SMLM imaging qualities. First, fixation with 4% PFA is commonly used in immunolabeling of corneal flatmount (Cho et al., 1990; Hiscott et al., 1997). Consistently, for the immunofluorescence staining of β-Tubulin, Vimentin, and PMP70 in endothelial cells on corneal flatmount, fixation with 4% PFA showed optimal staining qualities. In contrast, Histone-H4 fixed with 0.5% PFA showed the optimal results. The most important molecular change induced by aldehyde-based fixation is the cross-linking among proteins and nucleic acids (French and Edsall, 1945; Helander, 1994; Morgan et al., 1994; Werner et al., 2000). However, fixation with 4% PFA may lead to over fixation, especially for nuclear antigens (Nakashima et al., 2002). More specifically, the cross-linkings may result in masking of epitopes of Histone-H4 by altering the three-dimensional structure of proteins (Mason and O'Leary, 1991; Werner et al., 2000). Second, prolonged primary antibody incubation is required for the optimal staining quality. This was different from the routine staining protocols (i.e., 45 min to 1 h of each antibody incubation step) for SMLM of cultured cells even when stained with the same protein targets (Zhang et al., 2019). In this study, the optimized primary antibodies incubation time for β-Tubulin, Vimentin, and Histone-H4 were 48 h while PMP70 showed optimal results with 1-h incubation. We suspected both variations of different antigen-antibody affinities and antigen-exposure levels might impact the staining quality (Boenisch, 1999; Brandtzaeg, 1981; Ramos-Vara, 2005).

Using the optimized immunolabeling procedures, we showed super-resolution imaging of corneal flatmount using SMLM and sSMLM, particularly focused on endothelial and epithelial cells. The single-color SMLM images (Figs. 4 and 5) of the cornea tissue revealed greater nanoscale details of architectures and protein localizations that are unresolved by conventional fluorescence microscopy (Fig. 3A and B). Further, the sSMLM setup allows us to perform multi-color super-resolution imaging using only a far-red spectral channel with minimal cellular autofluorescence background (Fig. 6). This offers a better tool to study spatial interactions among multiple biomolecules simultaneously, even in tissue samples. Note that the optimal immunofluorescence protocols for β-Tubulin and Histone-H4 are different. To realize simultaneous two-color sSMLM imaging, we fine-tuned the concentration of PFA for retaining imaging qualities of both protein targets. Indeed, the simultaneous two-color sSMLM imaging of β-Tubulin and Histone-H4 in endothelial cells clearly showed their desired nanoscale morphologies and relative intracellular distributions with our optimized fixation condition shown in Figs. 3–5.

Through this study, we also identified three areas that should be further improved for acquiring high-quality sSMLM images of the mouse corneal flatmount. First, a universal immunostaining protocol compatible with staining multiple antigens in the same tissue sample should be identified. High-specificity primary antibodies tailored for this tissue or other specific labeling method (e.g., nanobodies, DNA-based probes) could potentially maximize the labeling efficiency and minimize non-specific labelings. We have tried primary antibody-AF647 conjugates (Santa Cruz); the corresponding SMLM imaging qualities were not optimal, likely because of the degraded labeling specificity. We believe that sSMLM can be applied to image the corneal tissues from various species (e.g., rabbit, rat, human) after specific optimization of the staining protocol for each particular tissue specimen. Second, SMLM has a relatively low imaging speed. It typically takes ~5–10 min to acquire sufficient single-molecule signals to reconstruct high-quality SMLM and sSMLM images, which makes it impractical to image large tissue areas. The development of brighter dyes with higher photoswitching duty cycles and better imaging processing methods to analyze densely-packed single molecule signals could improve SMLM's imaging speed. Lastly, in principle, the corneal samples can be imaged using our recently developed three-dimensional (3D) sSMLM technology (Song et al., 2019, 2020). However, this study focuses on establishing the optimal sample preparation protocols for sSMLM imaging of different molecular contrasts, where 3D and 2D sSMLM imaging provide identical information in this context.

5. Conclusion

We optimized immunofluorescence staining protocols for β-Tubulin, Vimentin, PMP70, and Histone-H4 in endothelial cells on corneal flatmount for SMLM and applied these protocols to imaging corneal epithelial cells. We also performed multi-color sSMLM imaging of the corneal flatmount to visualize subcellular structures with around 20-nm localization precision for the first time. sSMLM offers unique spatial resolution and multiplexing capability for imaging flat-mounted whole tissue and enables the visualization of subcellular structure in intact cells close resembling their native molecular status. With the identification of optimal staining quality for sSMLM, development of fluorescence labeling technology, and implementation of new optical design, multiplexed sSMLM imaging can be a powerful tool to investigate multi-molecular interactions and molecular pathways in flat-mounted whole tissues. More specifically, in the context of cornea imaging, sSMLM opens up the opportunity to study pathophysiological mechanisms relevant to, for example, ocular surface disease, Fuchs' corneal endothelium dystrophy, keratitis, etc.

Acknowledgment

National Science Foundation (NSF) (CBET-1706642 and EFMA-1830969); National Institutes of Health (NIH) (R01EY026078, R01EY028304, R01EY019949, R01GM139151, R01GM140478, and P41GM135018).

Appendix A. Supplementary data

Supplementary data to this article can be found online at https://doi.org/10.1016/j.exer.2021.108499.

References

Aldrich, B.T., Schloetzer-Schrehardt, U., Skeie, J.M., Burckart, K.A., Schmidt, G.A., Reed, C.R., Zimmerman, M.B., Kruse, F.E., Greiner, M.A., 2017. Mitochondrial and morphologic alterations in native human corneal endothelial cells associated with diabetes mellitus. Investig. Ophthalmol. Vis. Sci. 58, 2130–2138.

Anshu, A., Price, M.O., Price, F.W., 2012. Descemet's stripping endothelial keratoplasty: long-term graft survival and risk factors for failure in eyes with preexisting glaucoma. Ophthalmology 119, 1982–1987.

Barry, P.A., Petroll, W.M., Andrews, P.M., Cavanagh, H.D., Jester, J.V., 1995. The spatial organization of corneal endothelial cytoskeletal proteins and their relationship to the apical junctional complex. Investig. Ophthalmol. Vis. Sci. 36, 1115–1124.

Bashir, H., Seykora, J.T., Lee, V., 2017. Invisible shield: review of the corneal epithelium as a barrier to UV radiation, pathogens, and other environmental stimuli. J. Ophthalmic Vis. Res. 12, 305.

Bates, M., Huang, B., Dempsey, G.T., Zhuang, X., 2007. Multicolor super-resolution imaging with photo-switchable fluorescent probes. Science 317, 1749–1753.

Betzig, E., Patterson, G.H., Sougrat, R., Lindwasser, O.W., Olenych, S., Bonifacino, J.S., Davidson, M.W., Lippincott-Schwartz, J., Hess, H.F., 2006. Imaging intracellular fluorescent proteins at nanometer resolution. Science 313, 1642–1645.

Bhogal, M., Lwin, C.N., Seah, X.-Y., Peh, G., Mehta, J.S., 2017. Allogeneic Descemet's membrane transplantation enhances corneal endothelial monolayer formation and restores functional integrity following Descemet's stripping. Investig. Ophthalmol. Vis. Sci. 58, 4249–4260.

Boenisch, T., 1999. Diluent buffer ions and pH: their influence on the performance of monoclonal antibodies in immunohistochemistry. Appl. Immunohistochem. Mol. Morphol. 7, 300.

Bon, P., Linares-Loyez, J., Feyeux, M., Alessandri, K., Lounis, B., Nassoy, P., Cognet, L., 2018. Self-interference 3D super-resolution microscopy for deep tissue investigations. Nat. Methods 15, 449–454.
Bongiovanni, M.N., Godet, J., Horrocks, M.H., Tosatto, L., Carr, A.R., Wirthensohn, D.C., Ranasinghe, R.T., Lee, J.-E., Ponjavic, A., Fritz, J.V., 2016. Multi-dimensional super-resolution imaging enables surface hydrophobicity mapping. Nat. Commun. 7, 1–9.
Brandtzaeg, P., 1981. Prolonged Incubation Time in Immunohistochemistry: Effects on Fluorescence Staining of Immunoglobulins and Epithelial Components in Ethanol-And Formaldehyde-Fixed Paraffin-Embedded Tissues.
Chang, Y.K., Hwang, J.S., Chung, T.Y., Shin, Y.J., 2018. SOX2 activation using CRISPR/dCas9 promotes wound healing in corneal endothelial cells. Stem Cell. 36, 1851–1862.
Chen, B.-C., Legant, W.R., Wang, K., Shao, L., Milkie, D.E., Davidson, M.W., Janetopoulos, C., Wu, X.S., Hammer, J.A., Liu, Z., 2014. Lattice light-sheet microscopy: imaging molecules to embryos at high spatiotemporal resolution. Science 346.
Cheuk, W., Chan, J.K.C., 2004. Subcellular localization of immunohistochemical signals: knowledge of the ultrastructural or biologic features of the antigens helps predict the signal localization and proper interpretation of immunostains. Int. J. Surg. Pathol. 12, 185–206.
Cho, H.I., Covington, H.I., Cintron, C., 1990. Immunolocalization of type VI collagen in developing and healing rabbit cornea. Investig. Ophthalmol. Vis. Sci. 31, 1096–1102.
Creech, M.K., Wang, J., Nan, X., Gibbs, S.L., 2017. Superresolution imaging of clinical formalin fixed paraffin embedded breast cancer with single molecule localization microscopy. Sci. Rep. 7, 1–10.
Crossman, D.J., Hou, Y., Jayasinghe, I., Baddeley, D., Soeller, C., 2015. Combining confocal and single molecule localisation microscopy: a correlative approach to multi-scale tissue imaging. Methods 88, 98–108.
Davis, J.L., Dong, B., Sun, C., Zhang, H.F., 2018. Method to identify and minimize artifacts induced by fluorescent impurities in single-molecule localization microscopy. J. Biomed. Optic. 23, 106501.
Davis, Janel, Soetikno, Brian, Song, Ki-Hee, Zhang, Yang, Sun, Cheng, Zhang, Hao F., 2020. RainbowSTORM: an open-source ImageJ plugin for spectroscopic single-molecule localization microscopy (sSMLM) data analysis and image reconstruction. Bioinformatics 36, 4972–4974.
DelMonte, D.W., Kim, T., 2011. Anatomy and physiology of the cornea. J. Cataract Refract. Surg. 37, 588–598.
Dong, B., Almassalha, L., Urban, B.E., Nguyen, T.-Q., Khuon, S., Chew, T.-L., Backman, V., Sun, C., Zhang, H.F., 2016. Super-resolution spectroscopic microscopy via photon localization. Nat. Commun. 7, 1–8.
Edelhauser, H.F., 2006. The balance between corneal transparency and edema the proctor lecture. Investig. Ophthalmol. Vis. Sci. 47, 1755–1767.
Forest, F., Thuret, G., Gain, P., Dumollard, J.-M., Peoc'h, M., Perrache, C., He, Z., 2015. Optimization of immunostaining on flat-mounted human corneas. Mol. Vis. 21, 1345.
French, D., Edsall, J.T., 1945. The reactions of formaldehyde with amino acids and proteins. Adv. Protein Chem. 2, 6.
Große, L., Wurm, C.A., Brüser, C., Neumann, D., Jans, D.C., Jakobs, S., 2016. Bax assembles into large ring-like structures remodeling the mitochondrial outer membrane in apoptosis. EMBO J. 35, 402–413.
Hart, R.W., Farrell, R.A., 1969. Light scattering in the cornea. JOSA 59, 766–774.
He, Z., Campolmi, N., Ha Thi, B.-M., Dumollard, J.-M., Peoc'h, M., Garraud, O., Piselli, S., Gain, P., Thuret, G., 2011a. Optimization of immunolocalization of cell cycle proteins in human corneal endothelial cells. Mol. Vis. 17, 3494–3511.
He, Z., Campolmi, N., Thi, B.-M.H., Dumollard, J.-M., Peoc'h, M., Garraud, O., Piselli, S., Gain, P., Thuret, G., 2011b. Optimization of immunolocalization of cell cycle proteins in human corneal endothelial cells. Mol. Vis. 17, 3494.
He, Z., Forest, F., Gain, P., Rageade, D., Bernard, A., Acquart, S., Peoc'h, M., Defoe, D.M., Thuret, G., 2016. 3D map of the human corneal endothelial cell. Sci. Rep. 6, 1–14.
Helander, K.G., 1994. Kinetic studies of formaldehyde binding in tissue. Biotech. Histochem. 69, 177–179.
Henriksson, J.T., McDermott, A.M., Bergmanson, J.P.G., 2009. Dimensions and morphology of the cornea in three strains of mice. Investig. Ophthalmol. Vis. Sci. 50, 3648–3654.
Hess, S.T., Girirajan, T.P.K., Mason, M.D., 2006. Ultra-high resolution imaging by fluorescence photoactivation localization microscopy. Biophys. J. 91, 4258–4272.
Hiscott, P., Seitz, B., Schlötzer-Schrehardt, U., Naumann, G.O.H., 1997. Immunolocalisation of thrombospondin 1 in human, bovine and rabbit cornea. Cell Tissue Res. 289, 307–310.
Janson, B.J., Alward, W.L., Kwon, Y.H., Bettis, D.I., Fingert, J.H., Provencher, L.M., Goins, K.M., Wagoner, M.D., Greiner, M.A., 2018. Glaucoma-associated corneal endothelial cell damage: a review. Surv. Ophthalmol. 63, 500–506.
Jimenez, A., Friedl, K., Leterrier, C., 2020. About samples, giving examples: optimized single molecule localization microscopy. Methods 174, 100–114.
Jun, Y.W., Kim, H.R., Reo, Y.J., Dai, M., Ahn, K.H., 2017. Addressing the autofluorescence issue in deep tissue imaging by two-photon microscopy: the significance of far-red emitting dyes. Chem. Sci. 8, 7696–7704.
Kim, D., Zhang, Z., Xu, K., 2017. Spectrally resolved super-resolution microscopy unveils multipath reaction pathways of single spiropyran molecules. J. Am. Chem. Soc. 139, 9447–9450.
Kim, J., Wojcik, M., Wang, Y., Moon, S., Zin, E.A., Marnani, N., Newman, Z.L., Flannery, J.G., Xu, K., Zhang, X., 2019. Oblique-plane single-molecule localization microscopy for tissues and small intact animals. Nat. Methods 16, 853–857.
Klevanski, M., Herrmannsdoerfer, F., Sass, S., Venkataramani, V., Heilemann, M., Kuner, T., 2020. Automated highly multiplexed super-resolution imaging of protein nano-architecture in cells and tissues. Nat. Commun. 11, 1–11.
Laasmaa, M., Vendelin, M., Peterson, P., 2011. Application of regularized Richardson-Lucy algorithm for deconvolution of confocal microscopy images. J. Microsc. 243, 124–140.
Mason, J.T., O'Leary, T.J., 1991. Effects of formaldehyde fixation on protein secondary structure: a calorimetric and infrared spectroscopic investigation. J. Histochem. Cytochem. 39, 225–229.
Maurice, D.M., 1962. The Cornea and Sclera, Vegetative Physiology and Biochemistry. Elsevier, pp. 289–368.
McGowan, S., Edelhauser, H., Pfister, R., Whikehart, D., 2007. Stem cell markers in the human posterior limbus and corneal endothelium of unwounded and wounded corneas. Mol. Vis. 13, 1984–2000.
Mikhaylova, M., Cloin, B.M.C., Finan, K., Van Den Berg, R., Teeuw, J., Kijanka, M.M., Sokolowski, M., Katrukha, E.A., Maidorn, M., Opazo, F., 2015a. Resolving bundled microtubules using anti-tubulin nanobodies. Nat. Commun. 6, 1–7.
Mikhaylova, M., Cloin, B.M.C., Finan, K., van den Berg, R., Teeuw, J., Kijanka, M.M., Sokolowski, M., Katrukha, E.A., Maidorn, M., Opazo, F., Moutel, S., Vantard, M., Perez, F., van Bergen en Henegouwen, P.M.P., Hoogenraad, C.C., Ewers, H., Kapitein, L.C., 2015b. Resolving bundled microtubules using anti-tubulin nanobodies. Nat. Commun. 6, 7933.
Mimura, T., Joyce, N.C., 2006. Replication competence and senescence in central and peripheral human corneal endothelium. Investig. Ophthalmol. Vis. Sci. 47, 1387–1396.
Mlodzianoski, M.J., Curthoys, N.M., Gunewardene, M.S., Carter, S., Hess, S.T., 2016. Super-resolution imaging of molecular emission spectra and single molecule spectral fluctuations. PloS One 11.
Moon, S., Yan, R., Kenny, S.J., Shyu, Y., Xiang, L., Li, W., Xu, K., 2017. Spectrally resolved, functional super-resolution microscopy reveals nanoscale compositional heterogeneity in live-cell membranes. J. Am. Chem. Soc. 139, 10944–10947.
Morgan, J.M., Navabi, H., Schmid, K.W., Jasani, B., 1994. Possible role of tissue-bound calcium ions in citrate-mediated high-temperature antigen retrieval. J. Pathol. 174, 301–307.
Nakashima, K., Hagiwara, T., Yamada, M., 2002. Nuclear localization of peptidylarginine deiminase V and histone deimination in granulocytes. J. Biol. Chem. 277, 49562–49568.
Nasse, M.J., Woehl, J.C., 2010. Realistic modeling of the illumination point spread function in confocal scanning optical microscopy. J. Opt. Soc. Am. A Opt. Imag. Sci. Vis. 27, 295–302.
Nicovich, P.R., Owen, D.M., Gaus, K., 2017. Turning single-molecule localization microscopy into a quantitative bioanalytical tool. Nat. Protoc. 12, 453–460.
Ovesný, M., Křížek, P., Borkovec, J., Švindrych, Z., Hagen, G.M., 2014. ThunderSTORM: a comprehensive ImageJ plug-in for PALM and STORM data analysis and super-resolution imaging. Bioinformatics 30, 2389–2390.
Quiroz-Mercado, J., Ramírez-Velázquez, N., Partido, G., Zenteno, E., Chávez, R., Agundis-Mata, C., Jiménez-Martínez, M.C., Garfias, Y., 2016. Tissue and cellular characterisation of nucleolin in a murine model of corneal angiogenesis. Graefes Arch. Clin. Exp. Ophthalmol. 254, 1753–1763.
Ramos-Vara, J.A., 2005. Technical aspects of immunohistochemistry. Vet. Pathol. 42, 405–426.
Rust, M.J., Bates, M., Zhuang, X., 2006. Sub-diffraction-limit imaging by stochastic optical reconstruction microscopy (STORM). Nat. Methods 3, 793–796.
Salvador-Gallego, R., Mund, M., Cosentino, K., Schneider, J., Unsay, J., Schraermeyer, U., Engelhardt, J., Ries, J., García-Sáez, A.J., 2016. Bax assembly into rings and arcs in apoptotic mitochondria is linked to membrane pores. EMBO J. 35, 389–401.
Shih, K.C., Lam, K.S., Tong, L., 2017. A systematic review on the impact of diabetes mellitus on the ocular surface. Nutr. Diabetes 7 e251-e251.
Song, K.-H., Dong, B., Sun, C., Zhang, H.F., 2018. Theoretical analysis of spectral precision in spectroscopic single-molecule localization microscopy. Rev. Sci. Instrum. 89, 123703.
Song, K.-H., Zhang, Y., Brenner, B., Sun, C., Zhang, H.F., 2020. Symmetrically dispersed spectroscopic single-molecule localization microscopy. Light Sci. Appl. 9, 1–10.
Song, K.-H., Zhang, Y., Wang, G., Sun, C., Zhang, H.F., 2019. Three-dimensional biplane spectroscopic single-molecule localization microscopy. Optica 6, 709–715.
Spühler, I.A., Conley, G.M., Scheffold, F., Sprecher, S.G., 2016. Super resolution imaging of genetically labeled synapses in Drosophila brain tissue. Front. Cell. Neurosci. 10, 142.
Sridhar, M.S., 2018. Anatomy of cornea and ocular surface. Indian J. Ophthalmol. 66, 190.
Strauss, S., Nickels, P.C., Strauss, M.T., Sabinina, V.J., Ellenberg, J., Carter, J.D., Gupta, S., Janjic, N., Jungmann, R., 2018. Modified aptamers enable quantitative sub-10-nm cellular DNA-PAINT imaging. Nat. Methods 15, 685–688.
Suseela, Y.V., Narayanaswamy, N., Pratihar, S., Govindaraju, T., 2018. Far-red fluorescent probes for canonical and non-canonical nucleic acid structures: current progress and future implications. Chem. Soc. Rev. 47, 1098–1131.
Van den Bogerd, B., Dhubhghaill, S.N., Koppen, C., Tassignon, M.-J., Zakaria, N., 2018. A review of the evidence for in vivo corneal endothelial regeneration. Surv. Ophthalmol. 63, 149–165.
Werner, M., Chott, A., Fabiano, A., Battifora, H., 2000. Effect of formalin tissue fixation and processing on immunohistochemistry. Am. J. Surg. Pathol. 24, 1016–1019.

Xu, J., Ma, H., Ma, H., Jiang, W., Mela, C.A., Duan, M., Zhao, S., Gao, C., Hahm, E.-R., Lardo, S.M., 2020. Super-resolution imaging reveals the evolution of higher-order chromatin folding in early carcinogenesis. Nat. Commun. 11, 1–17.

Zhang, Y., Song, K.-H., Dong, B., Davis, J.L., Shao, G., Sun, C., Zhang, H.F., 2019. Multicolor super-resolution imaging using spectroscopic single-molecule localization microscopy with optimal spectral dispersion. Appl. Optic. 58, 2248–2255.

Zhang, Z., Kenny, S.J., Hauser, M., Li, W., Xu, K., 2015. Ultrahigh-throughput single-molecule spectroscopy and spectrally resolved super-resolution microscopy. Nat. Methods 12, 935–938.